

Response of the mode Grüneisen parameters with anisotropic compression: A pressure and temperature dependent Raman study of β -Sn

Jasmine K. Hinton ¹, Christian Childs,^{1,2} Dean Smith ^{1,3}, Paul B. Ellison ¹, Keith V. Lawler ⁴, and Ashkan Salamat ^{1,*}

¹*Department of Physics and Astronomy, University of Nevada, Las Vegas, Nevada 89154, USA*

²*Physical Life Sciences Directorate, Lawrence Livermore National Laboratory, P.O. Box 808, Livermore, California 94550, USA*

³*HPCAT, X-Ray Science Division, Argonne National Laboratory, Lemont, Illinois 60439, USA*

⁴*Department of Chemistry and Biochemistry, University of Nevada, Las Vegas, Nevada 89154, USA*



(Received 28 August 2020; revised 26 September 2020; accepted 2 November 2020; published 23 November 2020)

The lattice dynamic response of body-centered tetragonal β -Sn ($I4_1/amd$) under high-pressure and -temperature conditions is determined using experimental optical vibration modes. Raman scattering is used to map the phase stability region of β -Sn to perform mode Grüneisen analysis, and we demonstrate the necessity of an optical intensity calibration for Raman thermometry. The Grüneisen tensor is evaluated along a set of isotherms to address shortcomings of single-mode Grüneisen parameters with respect to anisotropic deformations of this tetragonal structured soft metal. The changes observed here in the Grüneisen tensor as a function of temperature are related to anharmonicity and denote potential criteria for the onset of premelting.

DOI: [10.1103/PhysRevB.102.184112](https://doi.org/10.1103/PhysRevB.102.184112)

I. INTRODUCTION

Direct measurement of warm, dense metals to probe their lattice dynamical properties has only recently been possible [1–6]. Main group metals straddle the boundary with non-metals and exhibit a large variation in orbital hybridization under high-pressure and -temperature conditions. This diversity in metallic bonding permits structural motifs more complicated than the simple metals [7]. As a result, discontinuous responses are to be expected for these soft metals as the melt is approached and their elastic properties respond to increases in bond anharmonicity. In elemental Sn, the brittle, low-temperature α -Sn phase (gray Sn) transitions into β -Sn (white Sn) via a colossal 20% volume collapse at 286 K [8]. The sp^3 hybridization of α -Sn is similar to lighter group 14 elements that adopt the diamond structure, whereas the sp hybridization of β -Sn behaves more like heavier, metallic Pb due to relativistic effects.

Tetragonal β -Sn ($I4_1/amd$) transforms into body-centered tetragonal (bct) γ -Sn ($I4/mmm$) above 10.8 GPa at 300 K [9]. The nature of this structural phase transition is first order and highly stress dependent, going to completion in a quasihydrostatic environment at 15.7 GPa. Upon further compression, a number of polymorphs with a body-centered and closed-packed lattice are revealed [9–11]. The melt line of Sn plateaus above 40 GPa, matching a discontinuous increase in the coordination number of liquid Sn [12,13]. Around 10–30 GPa and up to 1800 K, dynamic shock experiments across the β -Sn to γ -Sn transition have traversed the phase boundary with increases in reflectivity from 5% to 15% [14] and using time-resolved x-ray diffraction [15].

Raman spectroscopy provides a laboratory-bench method to optically probe the lattice dynamics of a material by the scattering of the phonon modes of the system. The main group soft metals, unlike many of the refractory transition metals, have Raman active phases; however, collecting Raman scattering from a metallic system such as β -Sn is still challenging owing to a low Raman scattering cross section [19,20] and a screening of low-energy excitations up to the plasma frequency of the metal. *Ab initio* simulations have estimated a plasma frequency of 8.3–9.2 eV for β -Sn [21], which has a polarization dependence from the anisotropy of the system and the Fermi level in a nonparabolic portion of the band structure [21–23]. Raman scattering is sensitive to electronically excited states as well as vibrational modes. Metals have several low-lying (visible, near-IR) electronic states that tend to be broader than their vibrational counterparts [20,24,25].

Despite the spectroscopic challenges discussed for working with metals, herein we present a detailed study of the P - T (Pressure-Temperature) stability region of β -Sn by Raman scattering, summarized in Fig. 1. The phase space is accessed using Ohmic heating in the diamond anvil cell (DAC) with the temperatures shown recorded from the thermocouple. A comparison of this temperature to Raman thermometry calculations can be found in Appendix B. Using the same Raman scattering data, we explore the effects of anisotropy in the calculation of the Grüneisen parameter and discuss the importance of reframing this parameter as a tensor.

II. METHODS

Sn (99.5% purity) metal shots from Spectrum Chemical with KBr as the pressure-transmitting medium were used in the high-pressure and -temperature experiments. CaCO_3 (99.9%) and $\text{SrB}_4\text{O}_7 : \text{Sm}^{2+}$ were used as temperature and pressure markers, respectively. [26]. Custom-designed DACs

*salamat@physics.unlv.edu

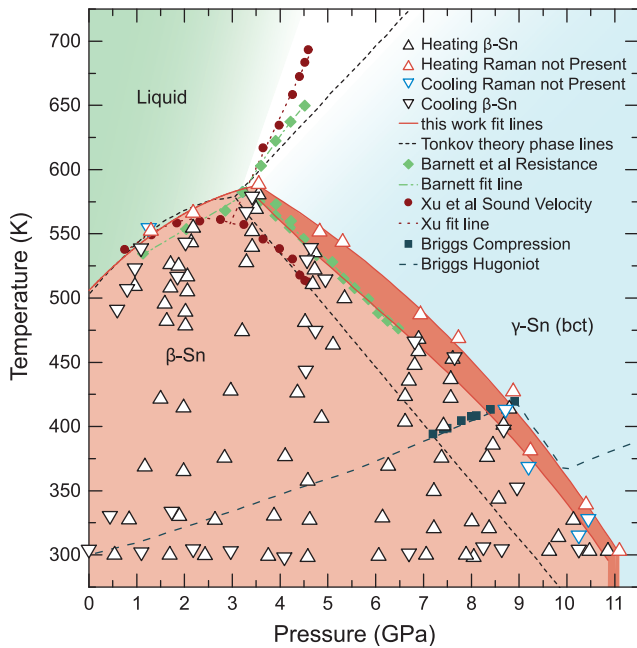


FIG. 1. Phase diagram of Sn showing the stability region of β -Sn obtained via Raman scattering. Open black triangles indicate the presence of β -Sn, while the colored triangles indicate its absence. Red is for a heating point, while blue is for a cooling point. The solid red lines are fits between the uppermost and lowermost points at which the Raman data no longer show β -Sn, and the dark red shaded region highlights this area between the two fit lines. The lighter shaded area guides the eye for the remainder of the stability region. Literature data in the legend can be found in Refs. [15–18].

and backing plates were equipped with 400- μ m culet diamonds. High-temperature conditions are reached through internal resistive heating, a technique in common use in diamond anvil cell research [27]. Using a ceramic with low thermal conductivity as a backing plate material contributed to greater thermal stability and control in our experiments. Further details on the resistive heating setup and backing plates can be found in Appendix A.

Raman spectroscopy was conducted on a home-built system using Optigrate volume Bragg gratings ($\lambda = 514.5$ nm). The characteristic fluorescence peak of $\text{SrB}_4\text{O}_7:\text{Sm}^{2+}$ was collected at each temperature interval. This pressure marker was chosen because its characteristic fluorescence is highly insensitive to temperature in our P, T region of interest between 0 and 12 GPa and below 600 K [28,29]. Measurements were taken only during heating runs once the sample was at a steady state within ± 1 K.

Plane-wave density functional theory (DFT) [30,31] simulations were performed with VASP 5.4.4. The strongly constrained and appropriately normed (SCAN) [32] meta-generalized gradient approximation functional was employed with a 250-eV plane-wave cutoff and a 10^{-8} -eV self-consistent field (SCF) tolerance. The valence $5s^25p^2$ Sn electrons were explicitly treated, and the Perdew-Burke-Ernzerhof [33] projector augmented wave [34] potentials were used to treat the core electrons. An automatically generated Γ centered Monkhorst-Pack grid with 0.15-\AA^{-1} spacing was

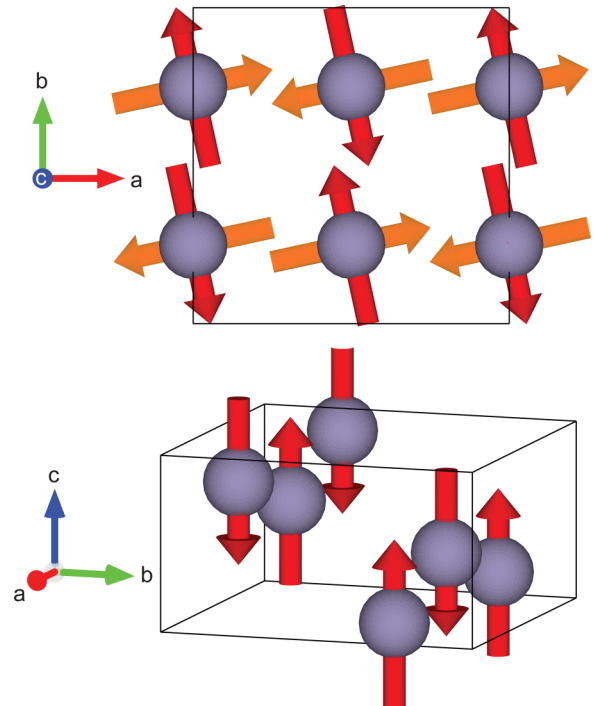


FIG. 2. The atomic displacements of the Raman active doubly degenerate E_g (top) and B_{1g} (bottom) modes of β -Sn ($I4_1/amd$).

used to sample the first Brillouin zone [35], which was integrated using the first-order Methfessel-Paxton scheme [36] with a 0.2-eV smearing width. Structural optimizations were constant pressure with all degrees of freedom allowed to change and forces converged within 10^{-3} eV/ \AA . Phonons were analyzed with PHONOPY [37] and calculated by 0.01- \AA finite displacements from a $3 \times 3 \times 4$ supercell to adequately sample the dispersion of the low-frequency acoustic phonons [38].

III. RESULTS AND DISCUSSION

A. The β -Sn stability dome

β -Sn in the second setting of the $I4_1/amd$ space group with atoms on the 4a Wyckoff positions has two allowed Raman modes. The complete irreducible representation is $\Gamma = B_{1g} + E_g + A_{2u} + E_u$ [39]. E_g and B_{1g} are optical modes responsible for the Raman scattering, while A_{2u} and E_u are acoustic modes in the IR and hyper-Raman region.

Figure 2 shows the atomic displacement vectors for the three Raman active optical modes of β -Sn; the displacements of the doubly degenerate E_g modes are confined to their respective $\{001\}$ (ab plane), and the displacements of the B_{1g} mode are along their respective $\langle 001 \rangle$ (c axis).

γ -Sn, a bct structure with atoms on the 2a Wyckoff positions, has the irreducible representation $\Gamma = A_{2u} + E_u$, which corresponds to two acoustic modes and no Raman active optical modes [39]. Because of the change in symmetry from β -Sn to γ -Sn, a sharp disappearance of Raman modes is observed in experiments. Figure 3(a) shows the presence of the two allowed Raman modes and their clear and distinct disappearance as the phase boundary between β -Sn and

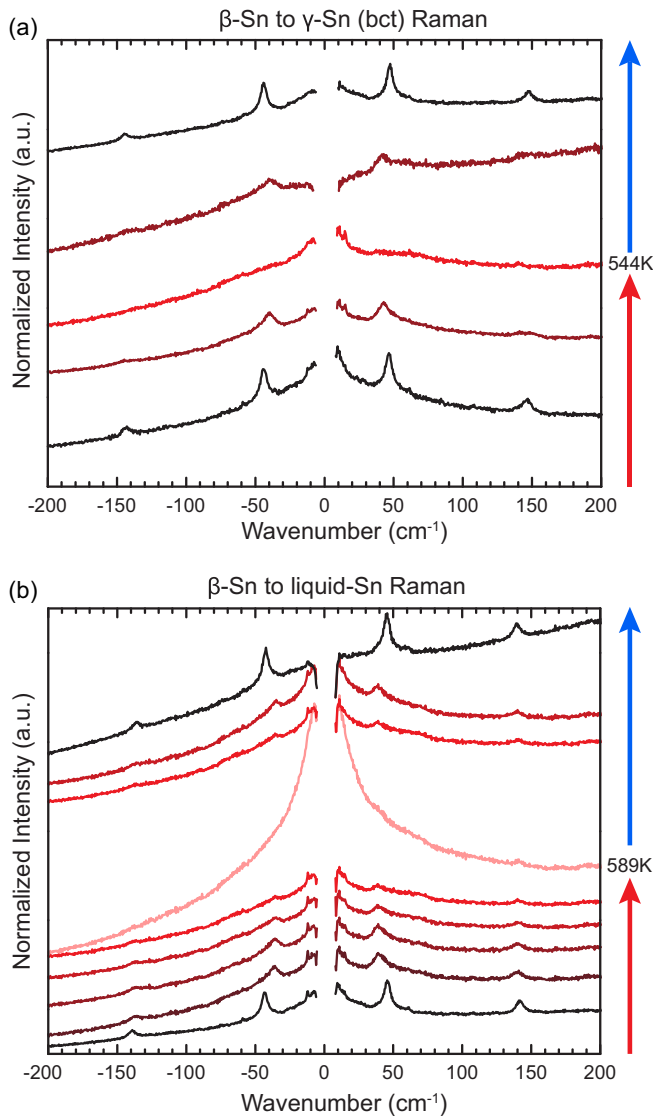


FIG. 3. Raman stack plots of Sn as a function of temperature under high pressure; ambient temperature up to the phase boundary at the listed temperature and then back to ambient. (a) As the β -Sn to γ -Sn line is crossed, a sharp disappearance in peaks is observed, with reappearance with decreasing temperature. Pressure ranges from 4.1 to 5.4 GPa throughout the heating and cooling process. (b) Raman modes broaden and decrease in intensity as the β -Sn melt line is approached. Pressure ranges from 2.1 to 3.4 GPa.

γ -Sn is traversed. This disappearance indicates that the phase fraction of β -Sn to γ -Sn has dropped below a detectable level for Raman scattering. We are unable to precisely map the confirmed phase coexistence from 10.8 to 15.7 GPa [9].

Approaching the β -Sn melt line, a broadening of Raman modes is observed, with the B_{1g} mode broadening more with temperature than the E_g mode. The relationship of the full width at half maximum intensity with temperature is fitted with a linear regression with a value of 0.007 for the E_g mode and 0.036 for the B_{1g} mode. Unlike the transition from β -Sn to γ -Sn, there is no sharp, discontinuous loss of Raman modes due to symmetry, but rather a progression towards a seemingly featureless Raman spectrum. In Fig. 3(b), we

observe a decrease in intensity of the two Raman modes of β -Sn as the melt line is approached. The relative intensity I/I_0 approaches but does not reach zero within error as the temperature increases toward the melt line. The broadening of peaks and decrease in intensity can be attributed to a loss of crystallinity during melting.

In Fig. 1, we compare our work to several previous studies and find agreement with literature trends and values. The reported triple point is considered at 583 K and 3.3 GPa [12,17,40], which is within our region of stability as determined by the thermocouple. Our melt transition data align with literature values [16,18], and we measure the stability region for β -Sn near the transition to γ -Sn extending to 11 GPa at 300 K. The Hugoniot compression and data points from [15] fall on our upper boundary of the stability region of β -Sn around 7–9 GPa, while the resistivity work of [17] lies on our lower boundary of the stability region from about 3 to 7 GPa. These upper and lower boundaries of stability do not include a mapping of the phase coexistence boundary with γ -Sn.

Temperatures obtained through Raman thermometry are compared to thermocouple temperatures in Appendix B (see Fig. 9). We find that the use of an independent, nonmetallic temperature marker improves the uncertainties of individual data points. The proper application of an optical transfer function (OTF) prevents dramatic systematic underestimations upwards of 22%. After applying an OTF to the system, the values obtained for temperature using Raman thermometry were systematically higher than the thermocouple values by 3%-10%. Although fair temperature stability was achieved by decreasing conductivity between the seats and the diamonds, some temperature gradient across the sample chamber likely still exists. Since the thermocouple measurements align well with accepted literature values for the phase diagram, particularly around the triple point, we rely on these data to establish the phase stability region. We include this and further discussion in Appendix B to highlight the challenges and limitations common to Raman thermometry under extreme conditions.

B. Mode Grüneisen analysis

The mode Grüneisen parameters connect the microscopic lattice vibrations of a material to its macroscopic thermodynamic properties. The mode Grüneisen parameter γ_i relates the response of a spectroscopically observable frequency ω_i of the i th phonon mode to a change in volume of the material [41]:

$$\gamma_i(\vec{q}) = -\left(\frac{\partial \ln \omega_i(\vec{q})}{\partial \ln V}\right)_T. \quad (1)$$

This is more conveniently defined for optical measurements like Raman scattering with excitation wavelengths in the visible in the long-wavelength ($\vec{q} \rightarrow 0$) limit as [42,43]

$$\omega_i/\omega_{i0} = [V/V_0]^{-\gamma_i}, \quad (2)$$

where ω_{i0} and V_0 are the phonon frequency and volume of the material at a reference state of the material, typically ambient conditions. Equation of state (EOS) analysis can provide the critical volumetric data for Grüneisen analysis, and several EOSs (Table I) have been determined for the room-temperature compression of β -Sn [9,44,45].

TABLE I. Pressure-volume equation of state of β -Sn at 300 K.

Equation of state	$V_p(V_0)$ (\AA^3)	$K_p(B_0)$ (GPa)	$K'_p(B'_0)$	Ref.
Birch-Murnaghan	27.06(1)	54.7(5)	4.5(1)	[9]
Murnaghan	27.0475	56.82	2.3	[45]
Birch	27.072	50.2 ± 0.5	4.9	[44]

The pressure evolution of the Raman active B_{1g} and E_g modes was measured and compared with the results of Olijnyk [46]. Nearly identical responses are observed for the E_g modes, and the B_{1g} modes differ only slightly. We attribute this to our improved Raman setup for measurements near the Rayleigh line. Each EOS from Table I produces a qualitatively similar Grüneisen parameter and pressure response when combined with our Raman data (Fig. 4); and these curves compare favorably to the previously reported ones of Olijnyk [46]. Figure 4 further shows that although the qualitative response of the mode Grüneisen parameter is similar, the choice of EOS model and data quality can change the given value for a pressure upwards of 16%.

Figure 5(a) shows Raman data expanded beyond room temperature, and the response of the modes is depicted against the unit cell volume, i.e., the dependent parameter of Grüneisen analysis. The pressure and temperature dependent unit cell volumes are determined from a large volume pressure dispersive x-ray diffraction (EDX) experiment [45]. It is immediately apparent that there is little to no temperature dependence for the E_g modes, whereas the B_{1g} mode shows a strong response to the temperature. Given that β -Sn is tetragonal, this response reflects a dependence on the anisotropy along an isochor (i.e. c/a ratio) for the B_{1g} mode, yet none for the E_g mode. Analysis of the EOS compression data shows that both the c and a axes compress monotonically with pressure. The c axis has a linear response to pressure, while the a axis has a higher-order response. In addition, the c axis has a somewhat uniform thermal expansion, but the a axis has a thermal expansion that effectively vanishes above 6 GPa. The different rates of compression and the thermal responses of the two axes are the source of the anisotropy along an isochor.

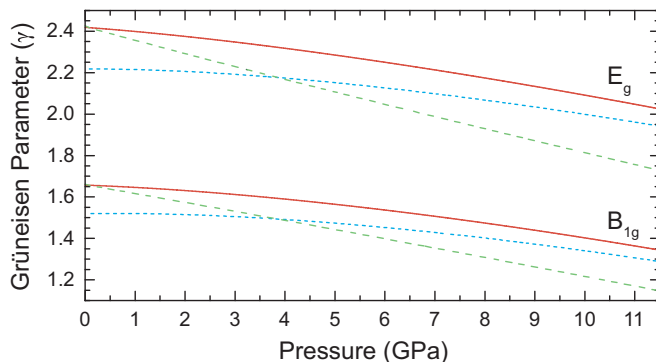


FIG. 4. The Grüneisen parameter as a function of pressure [Eq. (2)] using the fit to our measured frequencies and the equations of state of [9] (red), [45] (green), and [44] (light blue).

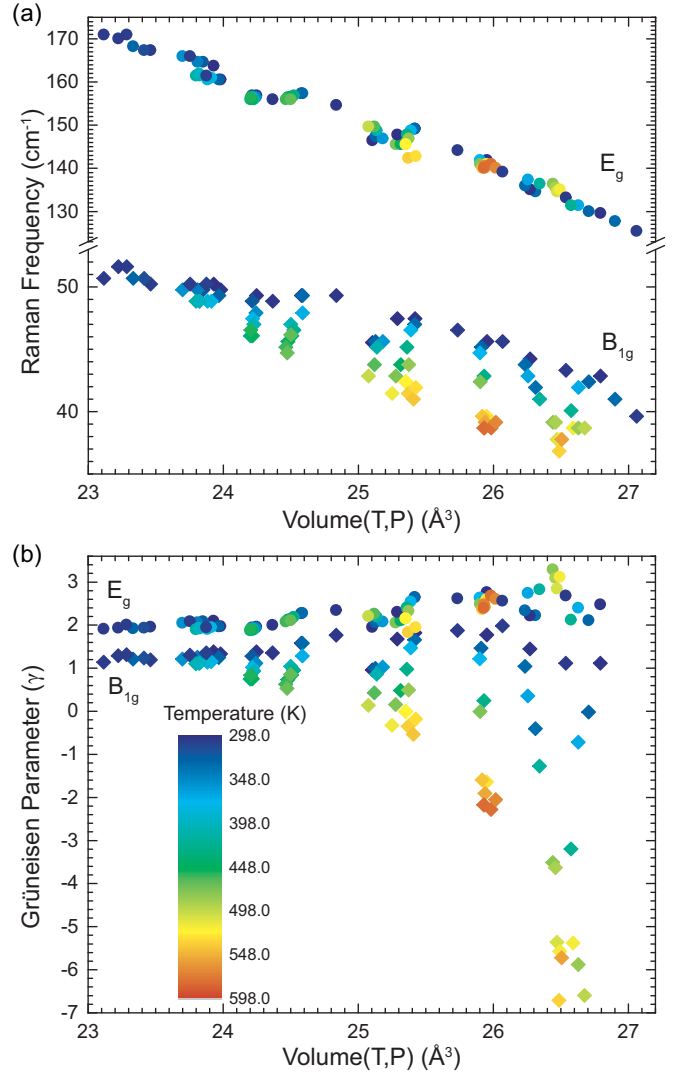


FIG. 5. (a) The frequency of the E_g (circles) and B_{1g} (diamonds) Raman active modes of β -Sn as a function of the temperature and pressure dependent unit cell volume. (b) The Grüneisen parameter as a function of the pressure and temperature dependent volume via Eq. (2).

Similarly incongruous behavior is seen when the temperature dependent Raman scattering is transformed into a Grüneisen parameter with Eq. (2) [Fig. 5(b)]. As with the room-temperature analysis, the Grüneisen parameter of the E_g modes shows a slight monotonic decrease upon compression. As anticipated from the Raman data, the higher-temperature Grüneisen parameters of the E_g modes show little temperature dependence. High-temperature points lie on top of the room-temperature data with only slight variance at higher volumes. On the other hand, the B_{1g} mode Grüneisen parameter goes from decreasing slightly with compression at room temperature to being negative valued and increasing with compression at elevated temperature. The lowest value of the B_{1g} mode Grüneisen parameter becomes more negative with increased temperature. The compressed value approaches the same limiting value regardless of temperature. Again, this

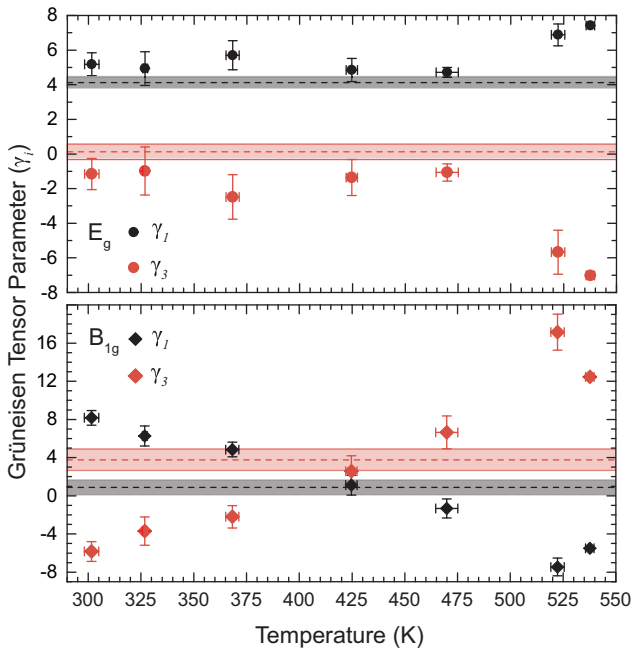


FIG. 6. Grüneisen tensor as a function of temperature plotted by mode and tensor component. Dashed lines represent the constant mode Grüneisen tensor with all data aggregated. Black is γ_1 and red is γ_3 . Top: E_g mode. Bottom: B_{1g} mode.

highly varying response of the B_{1g} mode displays its sensitivity to the anisotropic changes of the volume of β -Sn at different pressure-temperature conditions.

To better understand the response of the Raman modes to the anisotropy of β -Sn, the Grüneisen parameter can be decomposed into a tensor that follows the components of the strain tensor (in Voigt notation) [47]:

$$-\frac{\Delta\omega_i}{\omega_{0i}} = 2\gamma_{i1}\epsilon_1 + \gamma_{i3}\epsilon_3. \quad (3)$$

The symmetry of an orthorhombic cell removes the off-diagonal strain components. The tetragonal symmetry sets the strains in the X and Y directions equal: $\epsilon_1 = \epsilon_2$, $X \parallel a$, and $Z \parallel c$. The tensor representation of the Grüneisen parameter is not defined for a single pressure-temperature point, so the data were taken in aggregate. The infinitesimal Lagrangian strain [48] and Raman data were aggregated as described below, and then Eq. (3) was solved by ordinary linear least squares using the Moore-Penrose pseudoinverse. The thermodynamic paths traveled experimentally were roughly isobaric with both heating and cooling cycles. Only data collected during a heating cycle were considered for this analysis to avoid any issues with melt hysteresis in the aggregated data. The only exception is at 300 K where all data were included as the hysteresis loop should be closed with thermally equilibrated samples.

Early presentations of the anisotropic mode Grüneisen tensor were prefaced on the assumption that the tensor is constant valued like the macroscopic parameter [47]. When all of our data are aggregated, the resulting “constant” mode Grüneisen tensor components in Fig. 6 (horizontal dashed lines) intuitively follow the displacements shown in Fig. 2. The E_g

modes have a large γ_1 and near-zero γ_3 , corresponding to the atomic motion being constrained to $\{001\}$. The near-zero dependence on deformations of the c axis coupled with the lack of significant thermal expansion of the a axis at ≥ 6 GPa explains the temperature independence observed for the volumetric Grüneisen parameter of the E_g modes. Likewise, the B_{1g} mode has a larger γ_3 than γ_1 as the atomic motion is along $\langle 001 \rangle$. The smaller γ_1 of B_{1g} is much larger than γ_3 of the E_g modes (0.874 vs 0.122), reflecting the formers larger sensitivity to the anisotropic changes to the β -Sn structure.

Recently, it was shown that the idea of a single, constantly valued mode Grüneisen tensor does not follow the real behavior of a material. Thermally induced and pressure-induced changes to phonon mode frequencies are independent of one another and cannot be treated the same [49]. This requires that the mode Grüneisen tensor be evaluated isothermally at fixed temperatures across a series of data. To satisfy the constant temperature condition, we assembled data from different thermodynamic paths to create pseudoisotherms, as shown in Fig. 6. Vertical errors shown are calculated from the standard error of the ordinary least-squares fit of the Grüneisen tensor. Horizontal errors shown are the sample standard error of the mean temperature described by the pseudoisotherm. The standard error of the fit is large because this model constrains a value naturally varying with pressure (as illustrated in Fig. 4) to be a single value across all pressures for a given temperature. The variation of the Grüneisen tensor components with pressure is not an artifact of the anisotropic deformations of β -Sn. Even cubic materials like Li, Na, K, and Ge with isotropic deformations (and thus single-component Grüneisen tensors) still show a variance of $\gamma(P)$ with pressure [50,51].

Surprisingly, both modes start with a large γ_1 component at 300 K; for the B_{1g} mode, this is in stark contrast to the single global value. Initially, the components of the E_g modes’ Grüneisen tensor fluctuate nearly horizontally close to the predicted global value, supporting the concept of a constantly valued Grüneisen tensor. However, those components discontinuously diverge in opposite directions after 475 K, signaling some significant change to the system. Unlike the E_g components, the components of the Grüneisen tensor for the B_{1g} mode immediately start changing in opposite directions of each other. These differing initial responses are in line with the heightened sensitivity of the B_{1g} modes shown by the volumetric evaluation of the Grüneisen parameter [Fig. 5(b)]. However, a few observations in our results produce questions when compared to the atomic displacements shown in Fig. 2. For modes whose motions are constrained to only one direction described by the strain tensor, nonintuitively, there is a response of the tensor component in the other strain direction. Additionally, the B_{1g} mode starts with a larger response in a direction counter to its atomic motion, and the application of temperature seems to correct this. These observations lead us to consider that the bonding between the Sn atoms couples the different directions and changes with anisotropic deformations of the lattice.

Accurate DFT simulations can provide information about the bonding in the system to probe that hypothesis. The DFT optimized lattices of both end points (0 and 10.86 GPa) of the 300 K isotherm are within 3% of those obtained from the EOS. Phonon simulations confirm these structures are

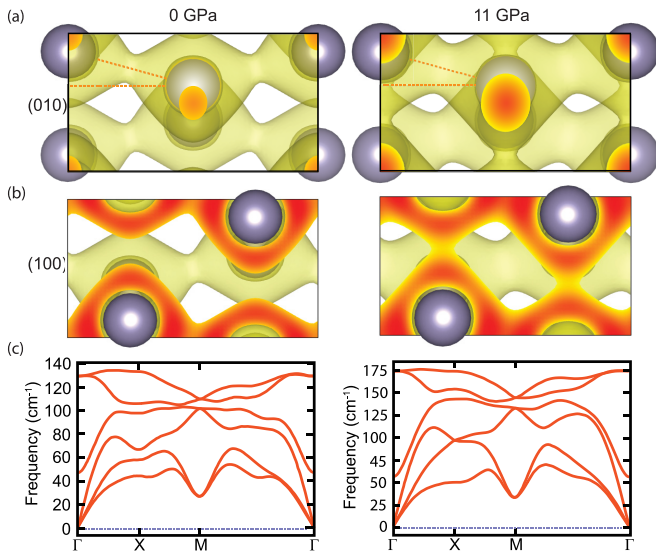


FIG. 7. The charge density of ambient (left) and compressed (right) β -Sn viewed along (a) [010] and (b) [100]. The 0.03 isosurface is shown in each instance. The angle a nearest-neighbor Sn-Sn bond makes with an ab plane is shown with a dashed line. (c) The phonon bands under the same conditions using the same k -point path as in [38].

dynamically stable (Fig. 7) and predict the frequencies (at the Γ point) of the three optical modes for each structure within 7.1 cm^{-1} of the experimental values (Table II). This level of agreement between DFT and experiment indicates a sufficiently accurate description of the electronic structure of β -Sn.

Turning to the bonding, Fig. 7 compares the electronic structure of β -Sn in the DFT optimized lattices at ambient and elevated conditions. The nonambient structure depicted is at 300 K and 10.86 GPa, but our simulations on other structures with similarly distorted c/a ratios are qualitatively similar. The charge density is polarized (nonspherical) around each of the Sn atoms, and at ambient conditions a significant covalency is observed only between a Sn atom and its four nearest neighbors at $\sim 3 \text{ \AA}$. These covalencies form a 15.40° (DFT, 15.29° experiment) angle with their respective $\{001\}$ (dashed lines in Fig. 7), and such a steep angle puts a majority component of each of these bonds into the respective ab plane. This geometry explains why the compression of the a and b axes is stiffer than that of the c axis, and why each mode has a larger initial sensitivity to ϵ_1 and ϵ_2 strains. As the c/a ratio shrinks

TABLE II. A comparison of the experimentally and DFT determined lattices and frequencies of the three optical Raman active modes of β -Sn at the end points of the 300 K isotherm.

	Pressure (GPa)	a (\AA)	c (\AA)	B_{1g} (cm^{-1})	E_g (cm^{-1})
Experiment	0.00	5.8321	3.1823	40.0	125.1
	10.86	5.5831	2.9663	52.1	171.0
DFT	0.00	5.8455	3.2196	47.1	129.6
	10.86	5.5784	3.0613	56.0	173.9

due to elevated pressure and/or temperature, the bond angles from the ambient structure shrink (15.34° for DFT and 14.88° for experiment in the case shown), placing a larger component of that bond in the direction of ϵ_1 and ϵ_2 . A new covalency forms between the Sn atoms stacked along $\langle 001 \rangle$ that appear weaker and happen at longer bond lengths than those present at ambient pressure and temperature. The emergence of these covalencies coupled with a nonvanishing component of the nearest-neighbor bonds in the $\langle 001 \rangle$ shows why the Grüneisen tensor shifts to favoring γ_3 (in terms of magnitude) while still retaining a non-negligible component in γ_1 .

From the bonding analysis, it is not apparent why the tensor components of the E_g modes diverge away from nearly horizontal behavior above 475 K, right after the different tensor components for the B_{1g} mode cross. It is known from lattice dynamics that harmonic approximations, like the one underlying Grüneisen parameter/tensor, break down about halfway to the melt [52]. Therefore, the discontinuity of the E_g modes' temperature dependent Grüneisen tensors is signaling an increased anharmonicity of the phonon modes. The increased anharmonicity will eventually trigger the system to melt [53]. The Grüneisen tensors indicate this by a rapid increase in magnitude with respect to temperature. We believe that the high sensitivity of the optically active phonon modes to the chemical environment of the system makes temperature-dependent mode Grüneisen tensor analysis a great tool for determining the onset of the premelt in a system. Additionally, it can be used as an alternative method for identifying melting when combined with an understanding of the Raman active modes of a liquid.

It should be noted that in the work presented here, all of the strains and changes in Raman frequency were determined against a single, global reference state at 0 GPa and 305 K. This reference state was measured in the DAC in order to maintain sample and data consistency throughout the entirety of the work. We attempted to use an individual reference state from within each pseudoisothermal data set, which is more in the spirit of the isothermal definition of the mode Grüneisen parameter [Eq. (1)]. That approach produced qualitatively the same curves as in Fig. 6 but with more nonmonotonic variance in magnitude. This variance could be from the cumulative error of combining our pressure-temperature measurements with those of the previous EDX study [45]. Future works should combine *in situ* x-ray diffraction (XRD) and Raman measurements for improved data fidelity and isothermal analysis.

IV. CONCLUSIONS

The phase stability of β -Sn was mapped under high-pressure and -temperature conditions using Raman scattering for phase determination and thermocouple data for temperature determination. The approach to the melt was marked by a broadening of the Raman features of β -Sn with an anisotropic temperature response for the two optical modes. The transition from β -Sn to γ -Sn was confirmed by the disappearance of Raman features associated with a change in symmetry. Our Raman spectral data, when combined with previously reported temperature dependent EDX structure data, allowed for a determination of the Raman response to structural

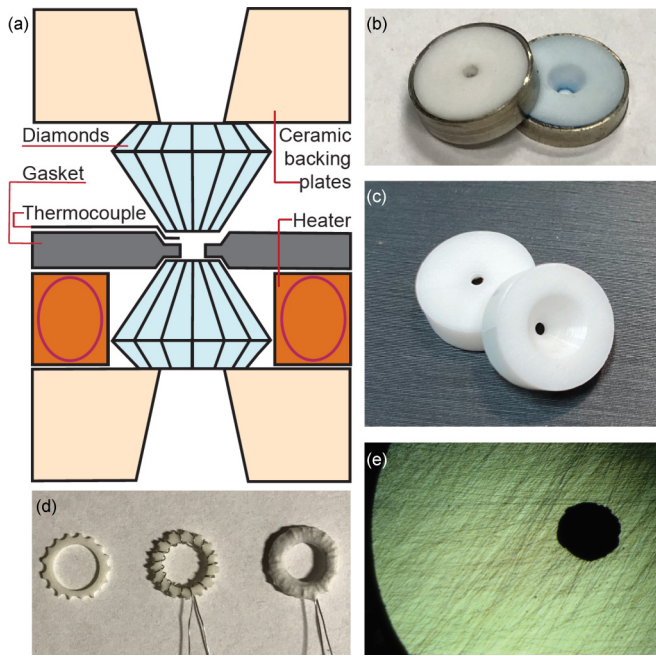


FIG. 8. Experimental configuration for Ohmic heating in the DAC. (a) Cross-sectional diagram of the DAC with heaters, ceramic backing plates, a gasket, diamonds, and thermocouple placement shown. (b) Photo of Macor backing plates with the steel protective ring. (c) Photo of the YSZ backing plates. (d) Photo of the resistive heaters including the ceramic ring with guiding grooves scored (left), a ring wound with nichrome heating wire (middle), and the wire-ring assembly covered in high-temperature cement (right). (e) Lapped YSZ surface.

changes via the Grüneisen parameter. Calculating a Grüneisen parameter for an anisotropic material like β -Sn does not fully capture the behavior of the material. Rather, calculating a Grüneisen tensor can give better insight into the connection between strain, atomic displacements, and temperature. Above 475 K, the values of the Grüneisen tensor diverge, indicating increased anharmonicity. Anharmonic behavior is known to lead to lattice instabilities at temperatures close to the melting temperature, and thus the calculation of the Grüneisen tensor could be helpful in identifying the onset of premelting in other systems. Calculating the mode Grüneisen tensor from Raman data in combination with simultaneous structural studies such as XRD and x-ray absorption spectroscopy, (which, to date, has not been done) will prove a powerful tool for the characterization of complex lattice dynamics of warm dense metals.

ACKNOWLEDGMENTS

We thank B. O'Donnell and R. Salem for useful discussions and protocol development. This work was supported by the U.S. Department of Energy, Office of Science, Basic Energy Sciences, under Award DE-SC0020303.

APPENDIX A: OHMIC HEATING

In this work, the heaters are made from 32-gauge Nichrome 60 wires wrapped around a ceramic guide ring and covered in

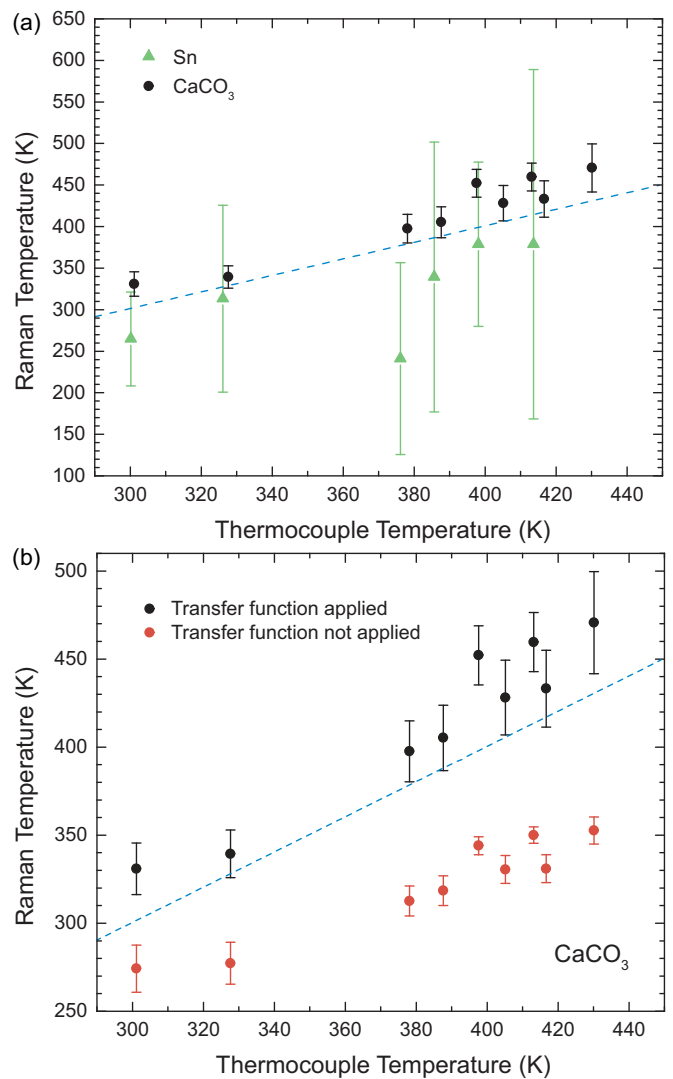


FIG. 9. The temperature as determined by Raman scattering vs the temperature determined by a thermocouple. Blue dashed lines represent equivalence. (a) Raman temperature calculation for CaCO_3 (black) compared to the Raman temperature calculation for β -Sn (green). (b) Raman temperature calculation for CaCO_3 comparing the application of a transfer function (black) vs the absence of a transfer function (red).

Resbond 940HT alumina adhesive high-temperature cement that shields the wire from oxidation damage and improves the thermal transfer to the gasket and sample. The cement is cured under vacuum. Figure 8(d) shows the preparation of a ceramic guide ring before and after winding with heating wire and then with a cement coating.

The heater sits in contact with the stainless-steel gasket inside the DAC. A K-type thermocouple is placed between the indentation of the gasket and the diamond and extends onto the culet near the sample chamber. Figure 8(a) shows a cross-sectional diagram of this experimental setup. Although the K-type thermocouple certainly experiences some strain effect as part of the experimental environment, we estimate that the result to the temperature measurement is likely within our reported experimental error bars.

Ceramic backing plates, machined in house from Macor, were used in these experiments. The thermal conductivity of Macor is much less than the commonly used backing plate material, tungsten carbide: 1.46 W/m K [54] compared to 110 W/m K [55], respectively. Using a lower thermally-conducting material as a backing plate works to lower heat transfer to the rest of the DAC and create a smaller, more isolated system between the heater, gasket, sample, and diamond in an effort to reach a thermal steady state [56]. Various resistive heating methods work to achieve this, including using one or more heaters of varying sizes, placements, and the use of vacuum chambers [57–59].

The use of thermally insulating ceramic materials as backing plates comes at the cost of tensile strength. Macor is susceptible to cracking during the alignment process, a problem easily fixed by machining a protective steel ring for the perimeter of the backing plate [shown in Fig. 8(b)]. While the Macor backing plates survive under loads required for pressure between 0 and 12 GPa with 400- μ m culets, they do not perform well under the load required for gasket indentations. Using yttria-strengthened zirconia (YSZ) as a backing plate material overcomes the problems of cracking on alignment without a metal protection ring and surviving higher indentation loads. A photo of our machined in-house YSZ backing plates is shown in Fig. 8(c). With a thermal conductivity of about 2–3 W/m K [60–62], comparably around a factor of 2 higher than Macor, YSZ serves as a thermal insulator in the same way Macor does; both materials' thermal conductivities are two orders of magnitude lower than that of tungsten carbide. Standard lapping techniques were used on both our Macor and YSZ backing plates in an effort to reduce surface roughness and improve surface embrittlement [63]; the lapped YSZ surface is shown in Fig. 8(e).

APPENDIX B: RAMAN THERMOMETRY

Temperature can be calculated from the frequencies and ratio of intensities of the Stokes vs anti-Stokes shifts of Raman active phonon modes [64,65]. From the Boltzmann distribution, the ratio of the intensity of the Stokes (S) and anti-Stokes (AS) shifts for phonon mode (i) is

$$\frac{I_S}{I_{AS}} = \frac{(\omega_0 - \omega_i)^4}{(\omega_0 + \omega_i)^4} \exp\left(\frac{\hbar\omega_i}{k_B T}\right). \quad (\text{B1})$$

ω_0 and ω_i represent the frequency of the Rayleigh line and frequency of mode i , respectively. k_B is Boltzmann's constant, and \hbar is Planck's reduced constant [66,67]. The intensities referred to in Eq. (B1) are measured in power (irradiance), which can be obtained from the CCD through a proper OTF converting photon counting to energy intensity. Without an OTF and considering only photon counts, the expression would be the same but with the prefactor raised to the third

power rather than the fourth [68]. The Boltzmann occupation increases for a mode with increased temperature, leading to I_S/I_{AS} approaching the limit of 1 as temperature goes to infinity. Due to the exponential dependence of I_S/I_{AS} on the mode frequency ω_i , the uncertainty in Eq. (B1) will approach unity faster for modes with low frequencies. Sn has Raman modes below 200 cm^{-1} which, because of the higher uncertainties, makes it a poor temperature marker. Additionally, since γ -Sn is not Raman active, it could not be used to calculate temperature beyond the transition to this phase.

To overcome this, a nonmetallic sample with a much greater Raman matrix element and a resulting larger scattering cross section can be used as an independent temperature marker. CaCO_3 fulfills this role with several intense modes well spaced in frequency, helping to maximize the sensitivity across the temperature range. Calcite and aragonite, two phases of CaCO_3 between 0 and 12 GPa, have extremely similar Raman spectra with modes at similar frequencies and intensities [69]. For this experiment three modes were used: two between 0–300 cm^{-1} , and one close to 1100 cm^{-1} . These modes were chosen for their frequency, spacing, and for their continued prominence throughout the experiment. Although prominent modes exist above 1100 cm^{-1} , this was a convenient wave number window to use experimentally in order to avoid the first-order Raman phonon line of diamond. Additionally, such high-energy anti-Stokes peaks would not be prominent enough to be useful until significantly higher temperature. Figure 9(a) compares the weighted average of the mode temperature calculation for Sn vs CaCO_3 ; larger uncertainties are present for Sn than for CaCO_3 , illustrating this inherent issue. Data were collected successively for Sn and CaCO_3 , hence the slight offset in temperature between them.

The basic error propagation used to calculate error bars in Fig. 9 revealed the uncertainties holding the highest weight were the intensities of the Stokes and anti-Stokes modes. In order to obtain meaningful absolute intensities, it is critical to perform an OTF to account for the quantum efficiency across the CCD detector as well as the response of the entire optical system. A NIST traceable tungsten bulb purchased from Oriol was used for the OTF in these experiments. Figure 9(b) shows the results of the comparison between a selection of CaCO_3 data with the application of an OTF and the same data set without the application of an OTF.

We emphasize that the use of an OTF is critical when using absolute intensities in cascading calculations. Since the OTF defines an efficiency offset for individual pixels across the detector, neglecting it will produce a nonsystematic error across the spectra and, by extension, the temperature calculation. Comparison of data at two temperatures from the same pixel does not negate the need for an OTF since this will not correctly assess the intensity and will produce an error in the temperature calculation for that pixel [64].

- [1] G. Aquilanti, A. Trapananti, A. Karandikar, I. Kantor, C. Marini, O. Mathon, S. Pascarelli, R. Boehler, and E. Tosatti, *Proc. Natl. Acad. Sci. USA* **112**, 12042 (2015).
 [2] Y. Ping, F. Coppari, D. G. Hicks, B. Yaakobi, D. E. Fratanduono, S. Hamel, J. H. Eggert, J. R. Rygg, R. F. Smith,

- D. C. Swift, D. G. Braun, T. R. Boehly, and G. W. Collins, *Phys. Rev. Lett.* **111**, 065501 (2013).
 [3] J. W. E. Drewitt, F. Turci, B. J. Heinen, S. G. Macleod, F. Qin, A. K. Kleppe, and O. T. Lord, *Phys. Rev. Lett.* **124**, 145501 (2020).

- [4] M. Frost, J. B. Kim, E. E. McBride, J. R. Peterson, J. S. Smith, P. Sun, and S. H. Glenzer, *Phys. Rev. Lett.* **123**, 065701 (2019).
- [5] R. Briggs, F. Coppari, M. G. Gorman, R. F. Smith, S. J. Tracy, A. L. Coleman, A. Fernandez-Pañella, M. Millot, J. H. Eggert, and D. E. Fratanduono, *Phys. Rev. Lett.* **123**, 045701 (2019).
- [6] F. Iesari, A. Trapananti, M. Minicucci, A. Filipponi, and A. Di Cicco, *Nucl. Instrum. Methods Phys. Res., Sect. B* **411**, 68 (2017).
- [7] S. I. Simak, U. Häussermann, R. Ahuja, S. Lidin, and B. Johansson, *Phys. Rev. Lett.* **85**, 142 (2000).
- [8] N. E. Christensen and M. Methfessel, *Phys. Rev. B* **48**, 5797 (1993).
- [9] A. Salamat, R. Briggs, P. Bouvier, S. Petitgirard, A. Dewaele, M. E. Cutler, F. Corà, D. Daisenberger, G. Garbarino, and P. F. McMillan, *Phys. Rev. B* **88**, 104104 (2013).
- [10] A. Salamat, G. Garbarino, A. Dewaele, P. Bouvier, S. Petitgirard, C. J. Pickard, P. F. McMillan, and M. Mezouar, *Phys. Rev. B* **84**, 140104 (2011).
- [11] A. Lazicki, J. R. Rygg, F. Coppari, R. Smith, D. Fratanduono, R. G. Kraus, G. W. Collins, R. Briggs, D. G. Braun, D. C. Swift, and J. H. Eggert, *Phys. Rev. Lett.* **115**, 075502 (2015).
- [12] R. Briggs, D. Daisenberger, O. T. Lord, A. Salamat, E. Bailey, M. J. Walter, and P. F. McMillan, *Phys. Rev. B* **95**, 054102 (2017).
- [13] R. Briggs, M. G. Gorman, S. Zhang, D. McGonegle, A. L. Coleman, F. Coppari, M. A. Morales-Silva, R. F. Smith, J. K. Wicks, C. A. Bolme, A. E. Gleason, E. Cunningham, H. J. Lee, B. Nagler, M. I. McMahon, J. H. Eggert, and D. E. Fratanduono, *Appl. Phys. Lett.* **115**, 264101 (2019).
- [14] B. La Lone, P. Asimow, O. Fat'yanov, R. Hixson, G. Stevens, W. Turley, and L. Veaser, *J. Appl. Phys.* **126**, 225103 (2019).
- [15] R. Briggs, R. Torchio, A. Sollier, F. Occelli, L. Videau, N. Kretschmar, and M. Wulff, *J. Synchrotron Radiat.* **26**, 96 (2019).
- [16] L. Xu, Y. Bi, X. Li, Y. Wang, X. Cao, L. Cai, Z. Wang, and C. Meng, *J. Appl. Phys.* **115**, 164903 (2014).
- [17] J. D. Barnett, R. B. Bennion, and H. T. Hall, *Science* **141**, 1041 (1963).
- [18] E. Y. Tonkov and E. G. Ponyatovsky, *Phase Transformations of Elements Under High Pressure* (CRC Press, Boca Raton, 2004), pp. 116–121.
- [19] Y. S. Ponosov and S. V. Streltsov, *Phys. Rev. B* **86**, 045138 (2012).
- [20] R. Carles, M. Bayle, P. Benzo, G. Benassayag, C. Bonafos, G. Cacciato, and V. Privitera, *Phys. Rev. B* **92**, 174302 (2015).
- [21] T. G. Pedersen, P. Modak, K. Pedersen, N. E. Christensen, M. M. Kjeldsen, and A. N. Larsen, *J. Phys.: Condens. Matter* **21**, 115502 (2009).
- [22] A. Svane and E. Antoncik, *Solid State Commun.* **58**, 541 (1986).
- [23] N. Christensen, *Solid State Commun.* **85**, 151 (1993).
- [24] M. Cazzaniga, L. Caramella, N. Manini, and G. Onida, *Phys. Rev. B* **82**, 035104 (2010).
- [25] G. V. Hartland, *Chem. Rev.* **111**, 3858 (2011).
- [26] SrB₄O₇ : Sm²⁺ was provided by Dan Frost at the University of Bayreuth.
- [27] L.-G. Liu and W. A. Bassett, *J. Geophys. Res.* **80**, 3777 (1975).
- [28] S. V. Rashchenko, A. Kurnosov, L. Dubrovinsky, and K. D. Litasov, *J. Appl. Phys.* **117**, 145902 (2015).
- [29] Q. Jing, Q. Wu, L. Liu, J. A. Xu, Y. Bi, Y. Liu, H. Chen, S. Liu, Y. Zhang, L. Xiong, Y. Li, and J. Liu, *J. Appl. Phys.* **113**, 023507 (2013).
- [30] P. Hohenberg and W. Kohn, *Phys. Rev.* **136**, B864 (1964).
- [31] W. Kohn and L. J. Sham, *Phys. Rev.* **140**, A1133 (1965).
- [32] J. Sun, A. Ruzsinszky, and J. P. Perdew, *Phys. Rev. Lett.* **115**, 036402 (2015).
- [33] J. P. Perdew, K. Burke, and M. Ernzerhof, *Phys. Rev. Lett.* **77**, 3865 (1996).
- [34] P. E. Blöchl, *Phys. Rev. B* **50**, 17953 (1994).
- [35] H. J. Monkhorst and J. D. Pack, *Phys. Rev. B* **13**, 5188 (1976).
- [36] M. Methfessel and A. T. Paxton, *Phys. Rev. B* **40**, 3616 (1989).
- [37] A. Togo and I. Tanaka, *Scr. Mater.* **108**, 1 (2015).
- [38] S.-H. Na, *J. Korean Phys. Soc.* **56**, 494 (2010).
- [39] E. Kroumova, M. L. Aroyo, J. M. Perez-Mato, A. Kirov, C. Capillas, S. Ivantchev, and H. Wondratschek, *Phase Transitions* **76**, 155 (2003).
- [40] J. D. Dudley and H. T. Hall, *Phys. Rev.* **118**, 1211 (1960).
- [41] F. D. Stacey and J. H. Hodgkinson, *Phys. Earth Planet. Inter.* **286**, 42 (2019).
- [42] B. Weinstein and R. Zallen, *Light Scattering in Solids*, edited by M. Cardona and G. Guntherodt (Springer, Berlin, 1984), Vol. 4.
- [43] J. E. Proctor, E. Gregoryanz, K. S. Novoselov, M. Lotya, J. N. Coleman, and M. P. Halsall, *Phys. Rev. B* **80**, 073408 (2009).
- [44] M. Liu and L.-g. Liu, *High Temp. High Press.* **18**, 79 (1986).
- [45] M. E. Cavaleri, T. G. Plymate, and J. H. Stout, *J. Phys. Chem. Solids* **49**, 945 (1988).
- [46] H. Olijnyk, *Phys. Rev. B* **46**, 6589 (1992).
- [47] R. J. Angel, M. Murri, B. Mihailova, and M. Alvaro, *Z. Kristallogr. - Cryst. Mater.* **234**, 129 (2019).
- [48] J. L. Schlenker, G. V. Gibbs, and M. B. Boisen Jr., *Acta Crystallogr., Sect. A* **34**, 52 (1978).
- [49] C. Stangarone, R. J. Angel, M. Prencepi, N. Campomenosi, B. Mihailova, and M. Alvaro, *Eur. J. Mineral.* **31**, 685 (2019).
- [50] R. Boehler, *Phys. Rev. B* **27**, 6754 (1983).
- [51] B. K. Pande, A. K. Pandey, and C. K. Singh, in *DAE Solid State Physics Symposium 2017, AIP Conf. Proc.* No. 1942 (AIP, New York, 2018), p. 120004.
- [52] J. D. Gale, *J. Phys. Chem. B* **102**, 5423 (1998).
- [53] Y. Ida, *Phys. Rev.* **187**, 951 (1969).
- [54] Corning, “Macor machinable glass”, <https://www.corning.com/media/worldwide/csm/documents/71759a443535431395eb34ebad091cb.pdf>.
- [55] K. Liu, X. P. Li, M. Rahman, and X. D. Liu, *Wear* **255**, 1344 (2003).
- [56] K. Yamamoto, S. Endo, A. Yamagishi, H. Mikami, H. Hori, and M. Date, *Rev. Sci. Instrum.* **62**, 2988 (1991).
- [57] N. Dubrovinskaia and L. Dubrovinsky, *Rev. Sci. Instrum.* **74**, 3433 (2003).
- [58] Z. Jenei, H. Cynn, K. Visbeck, and W. J. Evans, *Rev. Sci. Instrum.* **84**, 095114 (2013).
- [59] M. Santoro, A. Hajeb, and F. A. Gorelli, *High Pressure Res.* **40**, 379 (2020).
- [60] T. Shimonosono, T. Ueno, and Y. Hirata, *J. Asian Ceram. Soc.* **7**, 20 (2019).
- [61] K. W. Schlichting, N. P. Padture, and P. G. Klemens, *J. Mater. Sci.* **36**, 3003 (2001).

- [62] MSESUPPLIES, “ Description for yttrium stabilized zirconium oxide grinding/milling media”, https://www.msesupplies.com/products/12-7-mm-cylindrical-premium-yttria-stabilized-zirconia-ysz-milling-media?_vsrefdom=adwords&gclid=EAIaIqobChMI&variant=23685768904762.
- [63] C. J. Evans, P. D. Dornfeld, D. Lucca, G. Byrne, M. Tricard, F. Klocke, O. Dambon, and B. A. Mullany, *CIRP Ann.* **52**, 611 (2003).
- [64] M. Peña-Alvarez, P. Dalladay-Simpson, X. D. Liu, V. Afonina, H. C. Zhang, R. T. Howie, and E. Gregoryanz, *J. Appl. Phys.* **125**, 025901 (2018).
- [65] M. Oron-Carl and R. Krupke, *Phys. Rev. Lett.* **100**, 127401 (2008).
- [66] D. A. Long, *Raman Spectroscopy* (McGraw-Hill, New York, 1977).
- [67] D. A. Long, *The Raman Effect: A Unified Treatment of the Theory of Raman Scattering by Molecules* (Wiley, New York, 2002), Vol. 8, pp. 116–120.
- [68] J. J. Gallardo, J. Navas, D. Zorrilla, R. Alcantara, D. Valor, C. Fernandez-Lorenzo, and J. Martin-Calleja, *Appl. Spectrosc.* **70**, 1128 (2016).
- [69] P. Gillet, C. Biellmann, B. Reynard, and P. McMillan, *Phys. Chem. Miner.* **20**, 1 (1993).